ADVANCED OPTICAL MATERIALS
www.advopticalmat.de

Ultrafast UV Luminescence of ZnO Films: Sub-30 ps Decay Time with Suppressed Visible Component

Marilou Cadatal-Raduban, Jiří Olejníček,* Kota Hibino, Yuki Maruyama, Aneta Písaříková, Keito Shinohara, Toru Asaka, Lenka Lebedová Volfová, Michal Kohout, Zhang Jiaqi, Yugo Akabe, Makoto Nakajima, John A. Harrison, Rainer Hippler, Nobuhiko Sarukura, Shingo Ono, Zdeněk Hubička, and Kohei Yamanoi*

Ultrafast sub-100 picosecond luminescence is vital in many applications involving ultrafast events and time-of-flight systems. Materials exhibiting fast luminescence, such as barium fluoride (BaF_2) and zinc oxide (ZnO), also suffer from an intrinsically slow nanosecond (ns) to microsecond (µs) luminescence. Here, 2.2 micrometer (µm)- to 5.7 µm-thick undoped ZnO films on soda-lime glass (SLG) substrates without a buffer layer by a hybrid pulsed reactive magnetron sputtering operating in the medium-frequency range (MF magnetron) assisted by an electron cyclotron wave resonance (ECWR) plasma is deposited. The undoped ZnO films exhibited superior optical properties characterized by intense ultraviolet (UV) luminescence, unprecedented ultrafast decay times, and for the case of MF+ECWR-deposited films, suppressed defect-related visible luminescence. The 2.2 µm-thick MF-deposited film exhibited the fastest 9-ps decay time at room temperature. The impressive properties of the films are attributed to the use of advanced deposition technology with properly tuned plasma parameters, especially a high degree of dissociation of molecular oxygen together with an increased proportion of activated zinc particles, leading to a higher deposition rate, better crystallinity, fewer defects, and a lower proportion of oxygen vacancies. These films will pave the way toward the development of time-of-flight detectors, high-resolution nuclear imaging cameras, and high-rate ultrafast timing devices.

1. Introduction

Ultrafast luminescence from scintillator materials is sought after due to the rapidly increasing demands in ultrafast timing, high-resolution imaging, and particle discrimination using ionizing radiation such as high-energy photons, gamma rays, x-rays, neutrons and charged particles. Scintillators absorb the radiation and subsequently emit photons (called luminescence) in the ultraviolet or visible wavelength region, thereby converting the otherwise inaccessible radiation into light that can be detected by photodetectors. As such, scintillators play a crucial role as the intermediary material in radiation detectors. In many applications, fast picosecond (ps) luminescence decay time is sought after. Time-of-flight (TOF) detectors, TOF-positron emission tomography (TOF-PET), and nuclear fusion research, rely on the scintillator's fast decay time to discriminate different types of radiation that exist simultaneously. High-resolution nuclear imaging cameras and high-rate ultrafast timing devices also require scintillators with ps decay times.[1] Along with fast decay time, high light yield is needed for ease of detecting the luminescence signal. However, scintillator materials are limited to one feature or the other because of the trade-off between decay time and light yield. The problem of detecting the weak luminescence from a scintillator with low light yield can be solved by using multiple detector arrays.[2] However, the demand of ultrafast applications for less than 100 ps time resolutions,[3,4] largely influenced by the luminescence decay

M. Cadatal-Raduban
Unitec Institute of Technology
139 Carrington Road, Mount Albert, Auckland 1025, New Zealand
E-mail: mraduban@unitec.ac.nz

The ORCID identification number(s) for the author(s) of this article can be found under https://doi.org/10.1002/adom.202400377

DOI: 10.1002/adom.202400377

M. Cadatal-Raduban, K. Shinohara, Z. Jiaqi, Y. Akabe, M. Nakajima, N. Sarukura, K. Yamanoi
Institute of Laser Engineering
Osaka University
2–6 Yamadaoka, Suita, Osaka 565–0871, Japan

M. Cadatal-Raduban, J. A. Harrison
School of Natural Sciences
Massey University
Auckland 0632, New Zealand

time, has posed an all-important fundamental problem that is more difficult to solve. The luminescence from a scintillator originates from the energy-level transitions of excited electrons.[5] Therefore, it requires ultrafast processes within the material that result in ps luminescence decay times and detectable light yields. Rare earth-doped materials are the most popular luminescence emitters and scintillator materials. However, even for parity-allowed transitions coupled with energy-transfer and concentration quenching mechanisms, the fastest decay time achieved by rare earth-doped materials is only a few nanoseconds (ns),[6–8] not to mention the presence of persistent luminescence.[9] The core-to-valence band luminescence of barium fluoride (BaF_2) typically exhibits a 600-ps decay time, with further reduction to 94 ps being achieved using various means.[10–12] BaF_2 is therefore among the most widely used scintillator materials. However, an intrinsically present 400-ns self-trapped exciton luminescence limits the overall decay time, and its 190 nm vacuum UV core-to-valence band luminescence wavelength is difficult to measure as it requires a specialized photodetector operating in vacuum. Zinc oxide (ZnO) exhibits ps excitonic UV luminescence with a wavelength ≈380 nm. As such, ZnO has been investigated as a scintillator material. Upon excitation, the promotion of an electron from the valence band to the conduction band is quickly followed by the formation of free excitons within a few ps.[13] Annihilation of the free exciton via the radiative recombination of the loosely bound electron and hole pair results in the observed UV luminescence. Decay times in the range of 440–900 ps at room temperature is typical for a bulk ZnO crystal[14–17] although a 190-ps decay time was also reported for x-ray imaging applications.[18] Further reduction in decay time up to 74 and 15 ps was achieved by intentionally doping a ZnO crystal with iron and indium, respectively, but at the expense of unwanted decrease in light intensity.[18] Film counterparts of bulk luminescent materials are being developed to take advantage of the micro-columnar structure and nanoparticle grain size of films, allowing high spatial resolutions and faster decay times to be achieved.[19,20] A decay time of 200 ps was reported from epitaxial films fabricated on a sapphire substrate by a plasma enhanced molecular beam epitaxy (MBE) method[21] and 500 ps by pulsed laser deposition (PLD).[22] The fastest decay time reported from undoped ZnO films deposited by plasma deposition techniques is ≈74 ps, which is from films deposited on *c*-plane sapphire by radio frequency (RF)-magnetron sputtering in an argon and oxygen $Ar+O_2$ ambient atmosphere.[23]

J. Olejníček, A. Písaříková, L. Lebedová Volfová, M. Kohout, R. Hippler, Z. Hubička
Institute of Physics of the Czech Academy of Sciences
Na Slovance 2, Prague 8 182 00, Czech Republic
E-mail: olejn@fzu.cz

K. Hibino, Y. Maruyama, S. Ono
Department of Physical Science and Engineering
Nagoya Institute of Technology
Nagoya 466–8555, Japan

T. Asaka
Division of Advanced Ceramics
Nagoya Institute of Technology
Nagoya 466-8555, Japan

N. Sarukura
New Industry Creation Hatchery Center
Tohoku University
Sendai 980-8579, Japan

ZnO films are relatively economical to fabricate, and therefore it is used widely in industry. However, to have a decent UV luminescence intensity, ZnO films are typically fabricated on more expensive sapphire substrates or on a ZnO buffer layer to minimize strain from lattice mismatch.[24] For high-energy scintillator applications such as x-ray detection and imaging, the thickness of the film should be in the range of several μm to tens of μm to accommodate large penetration depths.[25] Such a requirement is time- and cost-prohibitive for standard thin film deposition technologies. Hence, almost all the literature on ZnO films investigated layers with nm thicknesses whereas μm-thick layers exhibited deleterious defects.[26] Also, an important consideration for ZnO is the broad luminescence in the visible wavelength region that is notoriously present due to defect states. This broad luminescence has a slow μs decay time[27,28] that is undesirable for ultrafast applications. For decades, strategies for suppressing this visible luminescence focused on the introduction of dopants, mostly accomplished in films grown by either the MBE or PLD techniques.[29] When introduced in the form of oxides, these dopants reduce oxygen vacancies that are partly responsible for the visible luminescence, especially the green luminescence. In this work, the defect states-related visible luminescence is suppressed in undoped μm-thick ZnO films deposited on soda lime glass (SLG) substrates without a buffer layer by using pulsed reactive magnetron sputtering operating in the medium-frequency range (MF magnetron) assisted by an electron cyclotron wave resonance (ECWR) plasma (MF+ECWR magnetron). Characterization of the optical properties of the ZnO films reveal superior optical properties characterized by intense ultraviolet (UV) luminescence, unprecedented ultrafast decay times, and for the case of MF+ECWR-deposited films, suppressed defect-related visible luminescence.

2. Results and Discussion

The schematic diagram of the MF+ECWR deposition system used in this work is shown in **Figure 1a**. The magnetron is connected to a bipolar pulse power supply operating at the medium frequency of 40 kHz. The MF magnetron is further supplemented by a water-cooled single-turn RF electrode inserted between the zinc target and the rotating substrate holder (see RF-ECWR electrode in Figure 1a) and by a Helmholtz coil located outside the chamber. The coil provides a static uniform magnetic field, chosen to be ≈1.7 mT oriented perpendicular to the direction of deposition, to bring the system into ECWR resonance.[30] Figure 1b shows a photograph of the burning discharge in MF+ECWR mode (left picture) and of the pure ECWR plasma when the magnetron is turned off (right picture). Among various thin film deposition techniques, MBE, metalorganic chemical vapor deposition (MOCVD), and physical vapor deposition (PVD) such as DC or RF magnetron sputtering are routinely used to produce high-quality ZnO films with RF magnetron sputtering having the advantage of process simplicity and low temperature deposition;[21,23] The advantage of ECWR-plasma PVD is the significantly increased degree of plasma ionization that allows the working pressure to be reduced below 0.05 Pa during deposition.[31] Low pressure is a prerequisite for the successful preparation of high-quality, high-purity semiconductor layers.[32,33]

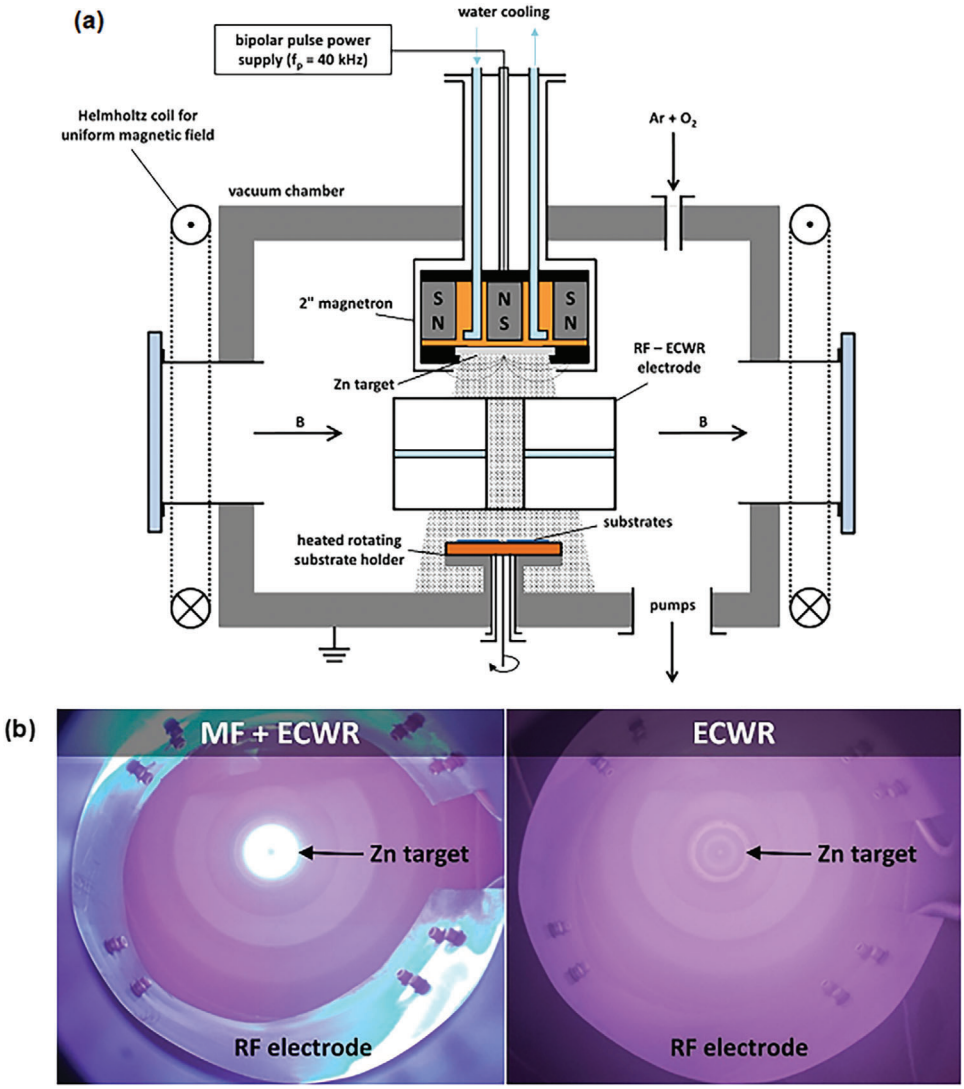

Figure 1. Design of the MF+ECWR deposition system. a) Schematic diagram of the vacuum chamber with the MF magnetron, RF-ECWR electrode and external Helmholtz coil used for the deposition of ZnO films. b) photograph of the burning discharge in the case of MF+ECWR (left) and pure ECWR (right), as viewed from the position of the substrate (i.e., from below). The photograph captures the typical violet argon plasma, the inner shell of the RF electrode and the magnetron zinc target, which is illuminated in the case of MF+ ECWR.

The grazing incidence x-ray diffractometry (GIXRD) spectra of representative films deposited by MF and MF+ECWR magnetron sputtering (**Figure** 2a) were all crystalline and exhibited diffraction peaks that can be indexed to the wurtzite structure of ZnO with *a* and *c* lattice parameters of 0.326 and 0.522 nm, respectively, and a preferred orientation in the (002) plane. For films of similar thickness, the films deposited by MF+ECWR have better crystallinity and bigger crystallite sizes compared to the films deposited by MF alone (Figure 2a). The difference in the crystallinity and crystallite size of the MF+ECWR and its counterpart MF film can be influenced by the difference in their thicknesses as the 2.2 µm thickness of the MF-deposited film is 73% of the 3.0 µm thickness of the MF+ECWR deposited film, and the 4.7 µm thickness of the MF deposited film is 82% of the 5.7 µm thickness of the MF+ECWR deposited film. Differences between the characteristics of the MF- and MF+ECWR-deposited films will be more evident when their Raman, photoluminescence and cathodoluminescence spectra will be compared. The crystallite size was determined using the Scherrer formula,

$$D = \frac{0.89\lambda}{B\cos\theta} \quad (1)$$

where λ is the 0.154 nm x-ray wavelength used during GIXRD measurement, θ is the diffraction angle of the peaks, and B is the full width at half maximum (FWHM) of the peaks. The degree of crystallinity quantified by the crystallinity index (CI) was determined from the ratio of the integrals of the crystalline phase contributions and the entire x-ray diffractogram that contains the combined crystalline and amorphous phase contributions. The crystalline phase contributions were determined by evaluating the area under the diffraction peaks. On the other hand, the

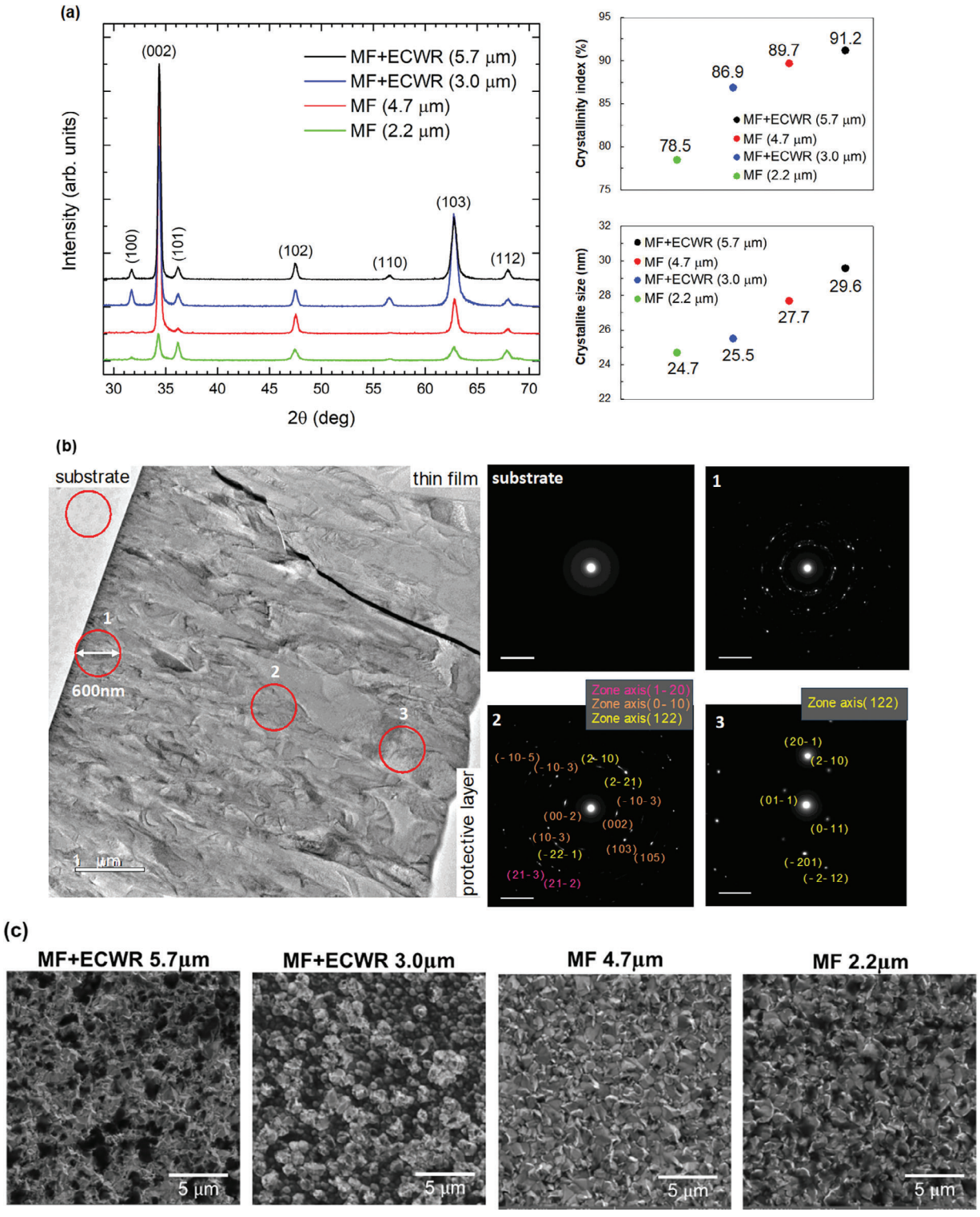

Figure 2. Morphological and structural analysis. a) GIXRD spectra of ZnO films deposited by MF with thicknesses of 2.2 μm (MF 2.2 μm), and 4.7 μm (MF 4.7 μm) and by MF+ECWR with thicknesses of 3.0 μm (MF+ECWR 3.0 μm), and 5.7 μm (MF+ECWR 5.7 μm). b) TEM diffraction patterns at different distances from the substrate. The surface orientation of the TEM electron diffraction images were analyzed using The International Centre for Diffraction Data – ICDD databases.[39] c) SEM images showing the surface morphology of ZnO films deposited by MF and MF+ECWR. The magnification of the SEM images is 10.4 kx. d) Raman spectra of the ZnO films deposited by MF and MF+ECWR, showing the typical ZnO normal modes at 99, 334, and 439 cm^{-1} (black fonts) and peaks associated with defects in the ZnO crystal at 277, 512, and 582 cm^{-1} (red fonts) that are present only in the films deposited by MF. e) Peak separation of the Raman spectrum using the positions of the known individual ZnO phonons. The peaks identified by white fonts in the graph are associated with normal modes of ZnO while the red fonts are associated with defects in the ZnO crystal and individual bonds.[36–38]

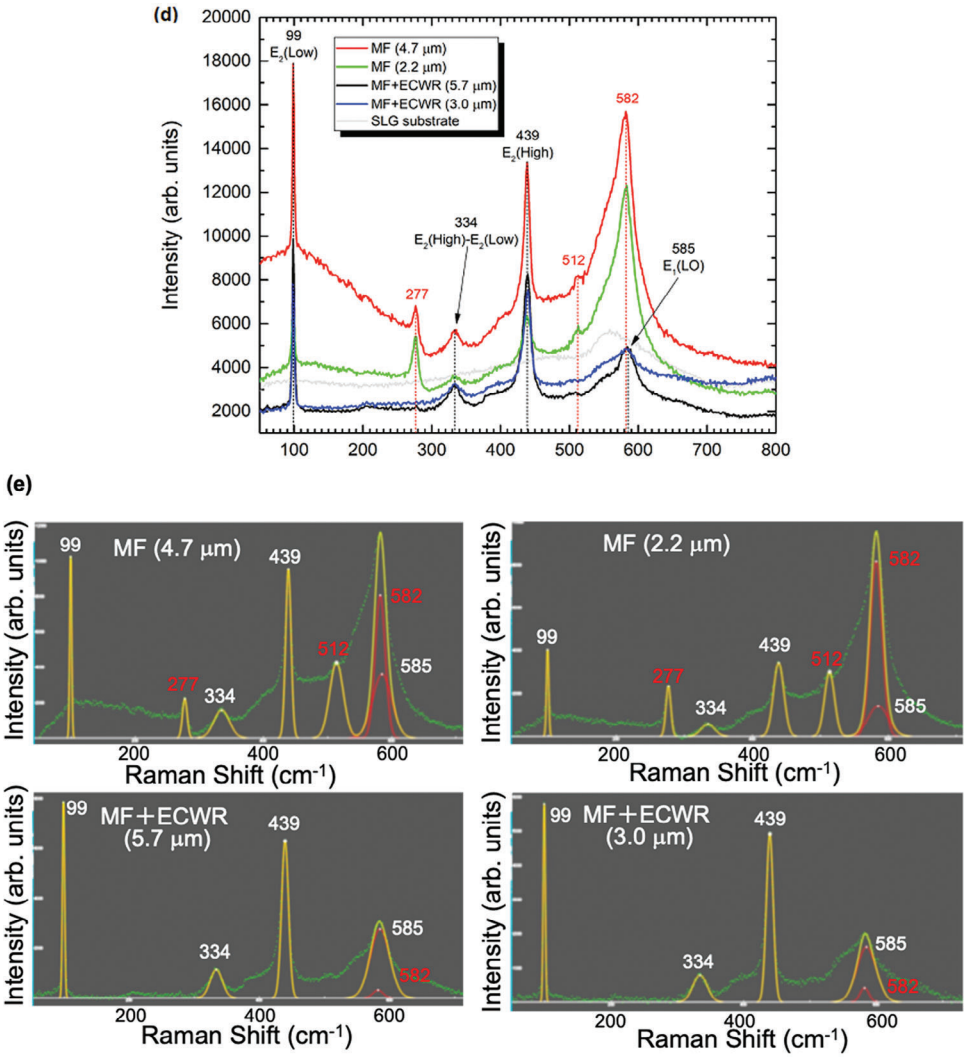

Figure 2. *Continued*

combined crystalline and amorphous contributions were determined by evaluating the area under the entire x-ray diffractogram.[34,35] The CI of the thinner film deposited by MF+ECWR (sample MF+ECWR 3.0 μm) is 86.9%, which is ≈10% better compared to its counterpart film deposited by MF (sample MF 2.2 μm) with a CI of 78.5%. The thicker films exhibited improved crystallinity and bigger crystallite sizes compared to the thinner films. The TEM diffraction pattern (Figure 2b) obtained from the cross-section of the thickest MF+ECWR 5.7 μm sample milled using a focused ion beam and at different distances from the substrate confirms the improvement in crystallinity as the thickness increases. The TEM diffraction pattern from the substrate (position labelled as substrate) clearly shows that the SLG substrate is amorphous. At position 1 where the deposited ZnO film is thin (≈600 nm thickness), the TEM diffraction pattern shows that it is polycrystalline characterized by a diffraction pattern of concentric rings in the zero order Laue zone. The rings within the diffraction pattern break and discrete reflections are observed as the thickness of the film increases (position 2 and position 3), indicating an increase in the crystallite size and the improvement in the crystallinity. The SEM images (Figure 2c) show that the films deposited by MF+ECWR are more porous and consist of oxide clusters while the films deposited by MF appear to be flat. This could be due to two reasons. First, the deposition rate for ZnO layers is ≈2x slower in MF compared to the deposition rate in MF+ECWR (55 nm min^{-1} for MF and 133 nm/min for MF+ECWR), and therefore the atoms on the surface are exposed to the environment for twice as long. This gives time for the incident atoms to migrate over the surface longer and form a less porous structure. Second, the chemical composition of plasma in MF and MF+ECWR are different. MF+ECWR contains far more dissociated oxygen atoms, which have a higher tendency to chemically react and form oxygen clusters on the surface of the ZnO layer. The atomic composition of the films was also measured by EDS. The measurement compositions were the same within the measurement uncertainty. The average oxygen content is ≈54%, which is slightly higher than the average zinc content of ≈46%. Figure 2d shows the Raman spectra of the films. In all the MF- and MF+ECWR-deposited films, the peaks at 99, 334, and 439 cm^{-1} (identified by black fonts in

the graph) are typical ZnO normal modes assigned to E_2 (Low), E_2 (High)-E_2(Low), and E_2 (High) modes, respectively.[36,37] In the films deposited by MF only, there are additional peaks at 277 and 512 cm^{-1} (identified by red fonts in the graph). These peaks are associated with defects in the ZnO crystal and individual bonds[36,38] Peak separation was performed on the broad peak from ≈560 to 640 cm^{-1}, revealing the presence of two peaks, one at 582 cm^{-1} and another at 585 cm^{-1} (see Figure 2e; Figure S1, Supporting Information). The peak at 585 cm^{-1} (identified by a white font in the graph) can be assigned to the E_1(LO) mode of ZnO[37] while the peak at 582 cm^{-1} (identified by a red font in the graph) is defect-related.[36,38] The separated peaks and intensity profiles in Figure 2e and Figure S1 (Supporting Information) show that for all the samples, the E_1(LO) normal mode of ZnO at 585 cm^{-1} is most intense in the MF+ECWR-deposited films, while the defect-related peak at 582 cm^{-1} is most intense in the MF-deposited films. By performing peak separation on the entire Raman spectrum as shown in Figure 2e, it can be concluded that the increase in the intensity of the broad peak containing both the 582 cm^{-1} defect mode and 585 cm^{-1} normal mode is mainly due to the increase in the intensity of the defect-related 582 cm^{-1} mode. This indicates, together with the defect related peaks 277 and 512 cm^{-1}, that bond failures are mainly associated with ZnO layers prepared by MF magnetron without ECWR and the MF-deposited films contain more defects compared to the MF+ECWR-deposited films. Both the GIXRD and Raman spectra confirmed that all four samples presented in this work are crystalline and have the same crystal structure regardless of the deposition conditions used during their deposition. Neither a shift in the position of the individual peaks in the XRD spectra nor a shift in the position of the phonon lines in the Raman spectra was observed, which indicates that there is neither a change in the dimensions nor a significant stress in the crystal lattice of the individual layers.

The photoluminescence (PL) spectra of the ZnO films excited by 290-nm fs laser pulses exhibited a UV luminescence peak centered ≈382 ± 0.1 nm, with no significant shift in the peak wavelength (**Figure 3a**). Since this UV peak is located near the fundamental absorption edge and is highly correlated with the bandgap of the films (Figure 3a; Figure S2, Supporting Information) and the 60 meV free exciton binding energy,[40,41] it is also referred to as near-band-edge (NBE) luminescence. The UV luminescence from the films deposited by MF+ECWR are significantly more intense compared to the films deposited by MF. The absolute PL quantum yield of the UV luminescence measured using a xenon lamp is 0.23% for MF+ECWR 5.7 µm, 0.20% for MF+ECWR 3.0 µm, 0.18% for MF 5.7 µm and 0.12% for MF 2.2 µm. The more intense luminescence is attributed to collaborative contributions of better crystallinity[42] (Figure 2a), improved transparency and lower self-absorption (Figure S2, Supporting Information) of the 382 nm PL emission for the MF+ECWR-deposited films compared to the MF-deposited films, particularly when comparing films with similar thicknesses. Self-absorption is the absorption of radiation by an object which it has itself emitted. In the case of the ZnO films, self-absorption pertains to the absorption of the 382-nm UV emission by the ZnO film itself. A higher absorption coefficient at 382 nm would mean that more of the 382-nm UV emission will be absorbed by the film, leading to a decrease in the emission intensity. Figure S2b (Supporting Information) clearly shows that the MF+ECWR (5.7 µm) film has the lowest absorption coefficient at 380 nm and therefore it exhibits the lowest self-absorption. The broad luminescence in the visible wavelength region, known to originate from defects (vacancies, interstitials, and their complexes) serving as luminescence centers, is more intense in the films deposited by MF (Figure 3b). The PL emission from the film deposited by MF is visibly red (Figure 3c). The smaller ratio of the visible to UV luminescence in the MF+ECWR-deposited films (Figure 3d) clearly indicate that combining MF with ECWR quenches the defect-related visible luminescence together with increasing the UV luminescence intensity, such that the films have similar intensity ratios to a bulk ZnO crystal with the same thickness as the MF+ECWR films. To verify this and to ascertain the type of defects in the films, the thickest MF and MF+ECWR films were cut to expose their cross-sections and polished by a cross section polisher (Figure S3, Supporting Information). The films were then excited cross-sectionally near the surface by a 5 keV electron beam. Exciting near the surface will probe the films at the similar depth excited by the 290-nm fs laser pulses. The irradiated area is 600 nm × 600 nm. The cathodoluminescence (CL) spectra (Figure 3e) confirms that the film deposited by MF+ECWR is characterized by an intense UV luminescence and a suppressed visible luminescence. Owing to the high energy of the electrons exciting the films in CL, multiple excitation paths are available and this results to different relaxation pathways that allows better access to the different defect-related states. Consequently, the CL spectra show higher visible luminescence compared to the PL spectra. Therefore, the CL spectra was used to evaluate and elucidate the origin of the visible luminescence. Deconvolving the CL spectra of the MF-deposited film using Gaussian functions reveals the presence of nine Gaussian curves representing constituent luminescence peaks (Figure S4 and Table S1, Supporting Information). The UV luminescence consists of a 369-nm (3.36 eV) NBE luminescence peak and a 376-nm (3.30 eV) excitonic luminescence peak. The excitonic and NBE luminescence peaks of the MF+ECWR-deposited films are narrower compared to those of the MF-deposited film (Table S1, Supporting Information). The MF-deposited films exhibited a larger area for all defect-related luminescence peaks. The MF+ECWR film clearly shows less intense defect-related luminescence, especially in the visible wavelength region where it is suppressed (Figure 3f and Table S1, Supporting Information). The peaks at 394, 420, 453, 496, 568, 620, and 670 nm originate from transitions involving zinc interstitials (Zn_i), oxygen interstitials (O_i), neutral oxygen vacancy (V_O), doubly ionized oxygen vacancy (V_O^{++}), and excess oxygen involving Zn vacancy complexes (V_{Zn}) (Figure 3g). The assignment of these peaks to the associated transitions involving the defect states is consistent with previous reports.[43–47]

The time-resolved spectra of the 380-nm UV PL peak obtained from streak camera images show luminescence profiles that exhibit a double exponential behavior with two decay components and feature ultrafast ps decay times, ranging from ≈27 ps (MF+ECWR) to as fast as 9 ps (MF) (**Figure 4a–j**). The UV PL from films deposited by MF is two to three times faster than those of the films deposited by MF+ECWR. We previously proposed that the two decay components in ZnO UV luminescence is related to crystal imperfections, where the fast decay component originates from regions with a high density of defects or

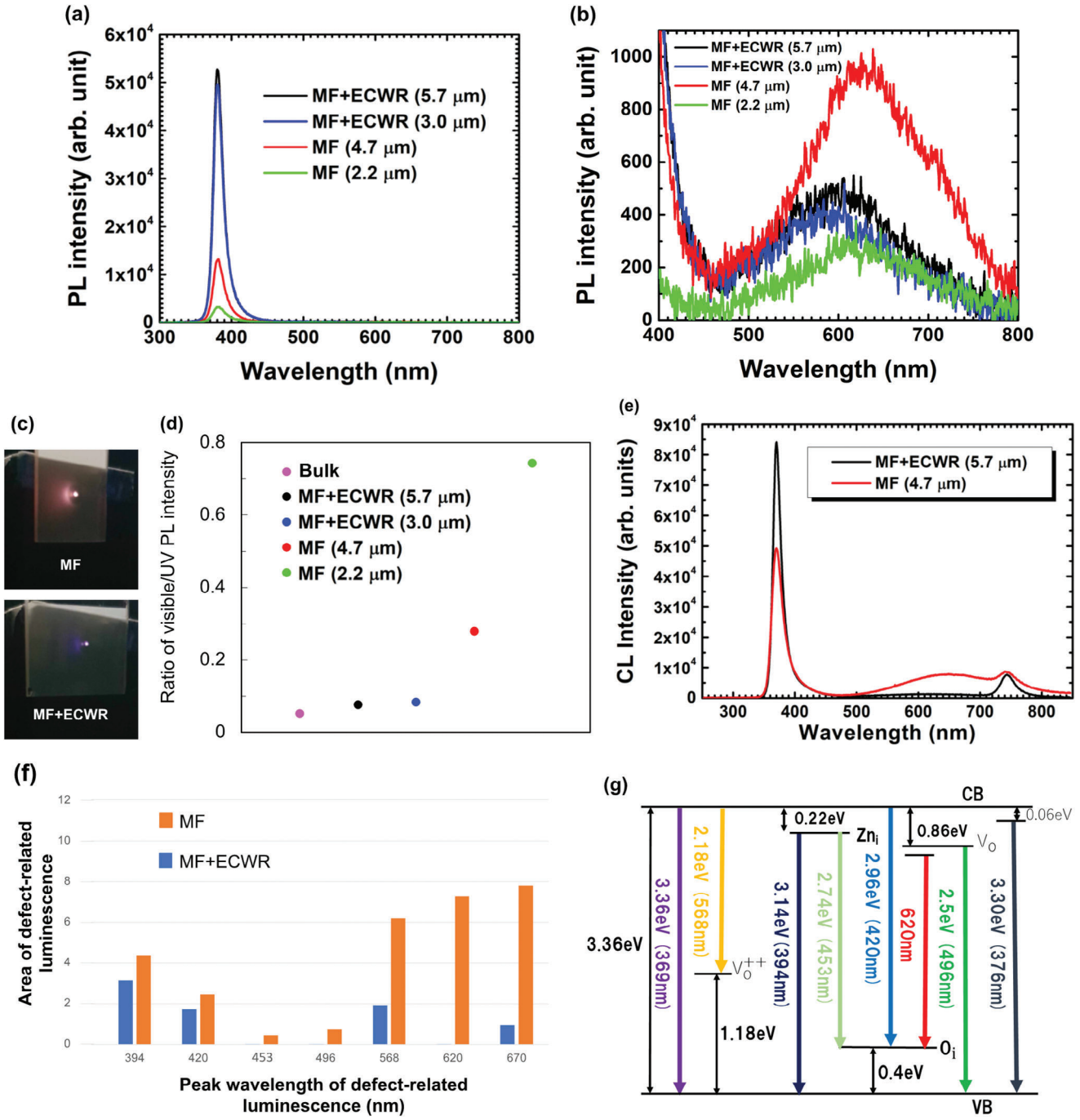

Figure 3. Probing the UV and visible luminescence in MF and MF+ECWR films. a) UV PL emission with peaks at 382.5 nm (3.241 eV) for MF 2.2 μm, 382.0 nm (3.246 eV) for both MF 4.7 μm and MF+ECWR 3.0 μm, and 381.5 nm (3.250 eV) for MF+ECWR 5.7 μm. All wavelength measurements have an uncertainty of ±0.1 nm. b) Visible PL emission. c) Photograph of MF- and MF+ECWR-deposited films excited by 290-nm fs laser pulses. d) Ratio of the visible to UV luminescence. A smaller number indicates lower visible luminescence intensity and/or higher UV luminescence intensity. e) CL spectra of the thickest MF and MF+ECWR films (MF 4.7 μm and MF+ECWR 5.7 μm samples) excited just below the surface of the films by a 5 keV electron beam. The peak ≈750 nm is the second order of the dominant UV luminescence peak. f) Comparison of the defect-related luminescence in MF and MF+ECWR films. The area is defined by the intensity and the full-width-at-half-maximum (FWHM) of the luminescence peak from Table S1 (Supporting Information). g) Energy level diagram showing transitions giving rise to the NBE luminescence peak (369 nm), excitonic luminescence (376 nm), and defect-related luminescence peaks.

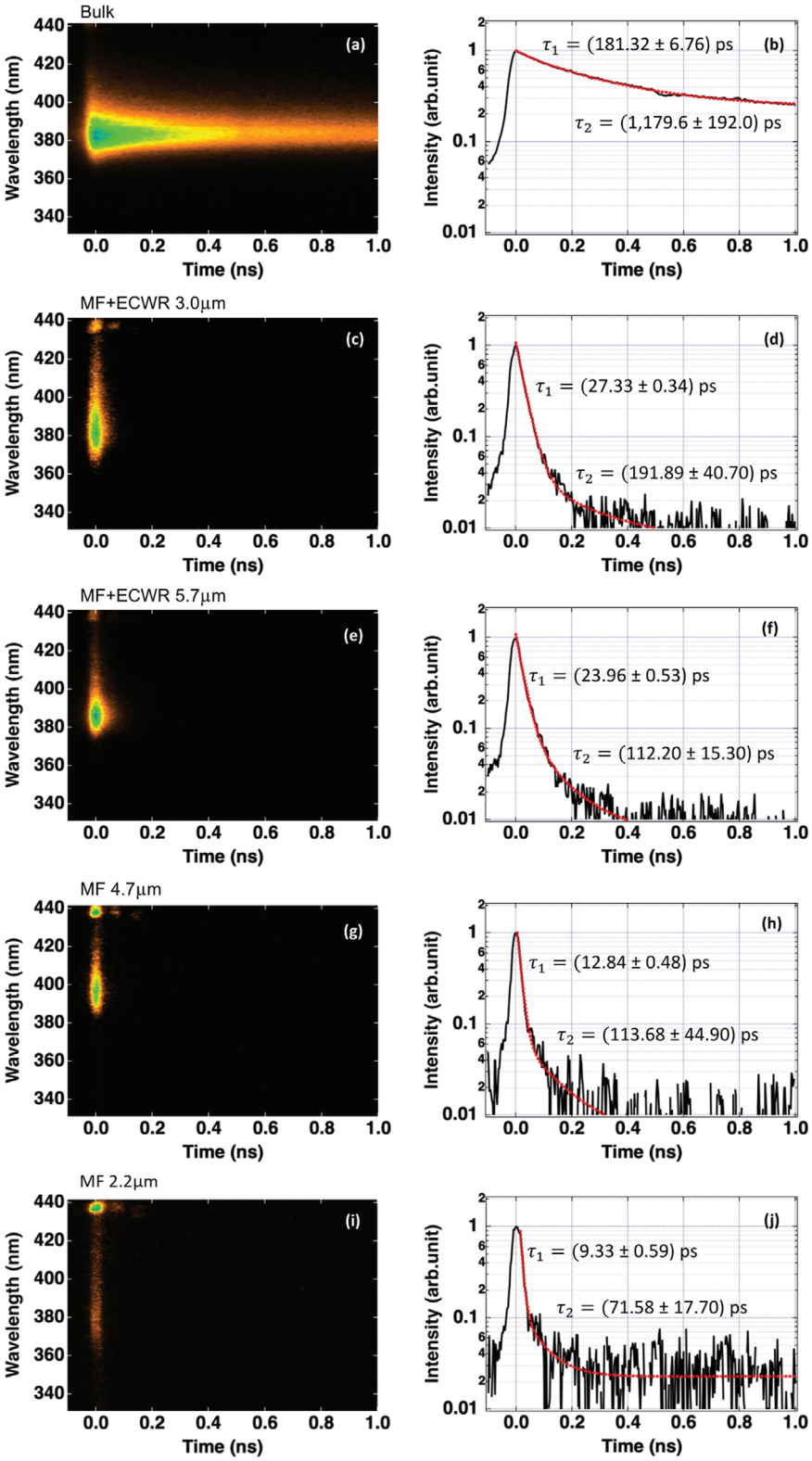

Figure 4. Ultrafast decay times from MF and MF+ECWR films. a), c), g), e), i), Streak camera images and b), d), f), h), j), Temporal profiles of the UV luminescence from a bulk ZnO crystal and thin films deposited by MF and MF+ECWR. The signal ≈435 nm is the residual second harmonic of the fundamental (870 nm) pulse of the Ti:sapphire laser.

impurities while the slow decay component is from regions with better crystallinity.[48] Non-radiative electron-hole recombination processes through impurities and defects are much faster compared to direct electron-hole radiative recombination. Therefore, the double exponential decay time of the UV PL peak can be analyzed in terms of electron-hole recombination through impurity and/or defect levels. If there is a high concentration of impurities and defects, then non-radiative recombination increases, and the decay time becomes faster. The greater number of Zn_i in the MF-deposited films resulting to the more intense 394-nm defect-related component of the UV luminescence obtained from the deconvolution of the UV CL peak (see peak number 3 in Figure S4, Supporting Information) increases the depopulation rate of excited electrons and decreases the lifetime of the free exciton, leading to a faster luminescence decay time. The streak camera and spectrograph system used to measure the time-resolved PL profiles has a temporal resolution of 10 to 15 ps.[18] Therefore, the fast 9-ps and 12-ps decay times of the MF-deposited films are limited by the temporal resolution of the measurement system and possibly could be even faster. Hence, we have realized unprecedented ultrafast decay times with intense UV and suppressed visible luminescence, satisfying the less than 100 ps time resolution requirement of ultrafast timing applications.

To understand the advantages of using the ECWR plasma in combination with MF magnetron sputtering, and hence elucidate the observed superior quality of the deposited ZnO films, we measured the plasma parameters directly during deposition of ZnO films using a modified RF probe,[49] capable of working in a highly reactive $Ar+O_2$ plasma and using optical emission spectroscopy (OES). We recorded and evaluated 3 sets of emission spectra and 3 sets of RF probe characteristics under different deposition conditions: i) pure MF, ii) MF+ECWR, and iii) ECWR alone without the MF magnetron discharge (Table S2, Figures S5 and S6, Supporting Information). Measurements of the plasma parameters using the RF probe reveal that the electron temperature (T_e) in the MF plasma is higher and has a different distribution function compared to the T_e in the ECWR and MF+ECWR plasma. The T_e measured in the pure ECWR and MF+ECWR plasmas are 2.6 and 3.9 eV, respectively while the pure MF plasma has two different groups of electrons: the cold group with T_e of 3.2 eV and the hot group with T_e of 27 eV, resulting to a higher effective T_e. The RF probe measurements also reveal that the ion density in the MF+ECWR plasma is almost two times higher compared to the ion density in the MF plasma (8.4×10^{16} m^{-3} vs 4.9×10^{16} m^{-3}). These two findings have a significant impact on the dissociation, excitation, and ionization processes in the plasma. The relatively dense but "cold" ECWR plasma will significantly contribute to the dissociation of oxygen (O_2) molecules (the bond-dissociation energy of O_2 molecules is 5.15 eV) and to the excitation and ionization of Zn atoms (the ionization energy of Zn atoms is 9.39 eV). However, the effect of ECWR on the ionization of argon atoms (Ar) and excitation of argon ions (Ar^+) will be significantly smaller, because the ionization energy of Ar is 15.76 eV. These are confirmed by the optical emission spectra (**Figure 5**). There is a strong increase in the intensity of all Zn lines (both neutrals and ions), which is more obviously seen from the spectra in Figure 5a,b, because of the excitation and ionization of Zn atoms being enhanced inside the ECWR plasma. The intensity of the emission lines of Ar neutrals also increased (Figure 5b), but the Ar^+ lines remained practically the same in both the MF and MF+ECWR plasmas. The significant contribution of ECWR to the dissociation of O_2 molecules is confirmed by the oxygen triplet at 777 nm consisting of the three closely-spaced lines 777.19, 777.42, and 777.54 nm lines (Figure 5c), whereby the intensities of all neutral oxygen lines in the ECWR plasma are more than three times higher than in the pure MF plasma despite the flow rate of O_2 gas being kept constant for all the experiments. This is a very important finding because atomic oxygen is a very reactive chemical species that behaves as a free radical. Therefore, this atom does not exist naturally for even a short period of time, and it tends to react immediately with other chemical elements or compounds. A high degree of dissociation of molecular oxygen together with an increased proportion of activated zinc particles contributes not only to a higher deposition rate of ZnO in the MF+ECWR magnetron, but especially to better crystallinity, fewer defects, and a lower proportion of oxygen vacancies. We have described a similar influence on the effectiveness of reactive sputtering for TiO_2 films, where we used a surfatron discharge as an additional plasma source for the dissociation and activation of oxygen species.[50] In that work, oxygen plasma pre-dissociation led to better reactivity of oxygen particles with the metal precursor, more accurate stoichiometry of the resulting TiO_2 films and better crystallinity.

The above results demonstrate that medium-frequency magnetron assisted by an electron cyclotron wave resonance plasma is a very advanced deposition technology capable of producing extremely high-quality ZnO layers with extraordinary properties. With optimally set plasma parameters that fit well into a relatively narrow process window, we were able to deposit µm-thick ZnO layers with impressive optical properties on inexpensive glass substrates. These optical properties were achieved without using expensive sapphire substrates or a ZnO buffer layer and even without dopant ions. The films exhibited good crystallinity and transparency especially in the UV wavelength region. We have realized intense UV luminescence with record fast decay times. More importantly, we have suppressed the unwanted defect-related visible luminescence. These collectively satisfy the requirements for ultrafast timing applications while eliminating the need for filters to screen out the slow visible luminescence. The ability of MF+ECWR to quench the visible luminescence can be capitalized further to achieve purely UV luminescence with even faster decay times, for instance by doping the films with gallium, iron, or indium.

3. Conclusion

In conclusion, 2.2- to 5.7 µm-thick undoped ZnO films were successfully sputtered on SLG substrates without a buffer layer by the MF and MF+ECWR plasma deposition techniques. Although the films were all crystalline with a wurtzite structure, the films deposited by MF+ECWR have better crystallinity and bigger crystallite sizes compared to the films deposited by MF alone. In terms of surface morphology, the MF+ECWR-deposited films are more porous consisting of oxide clusters. This could be due to the faster deposition rate of MF+ECWR and the higher concentration of dissociated oxygen atoms during MF+ECWR deposition. The near-band-edge UV photoluminescence and cathodoluminescence emission from the films deposited by MF+ECWR

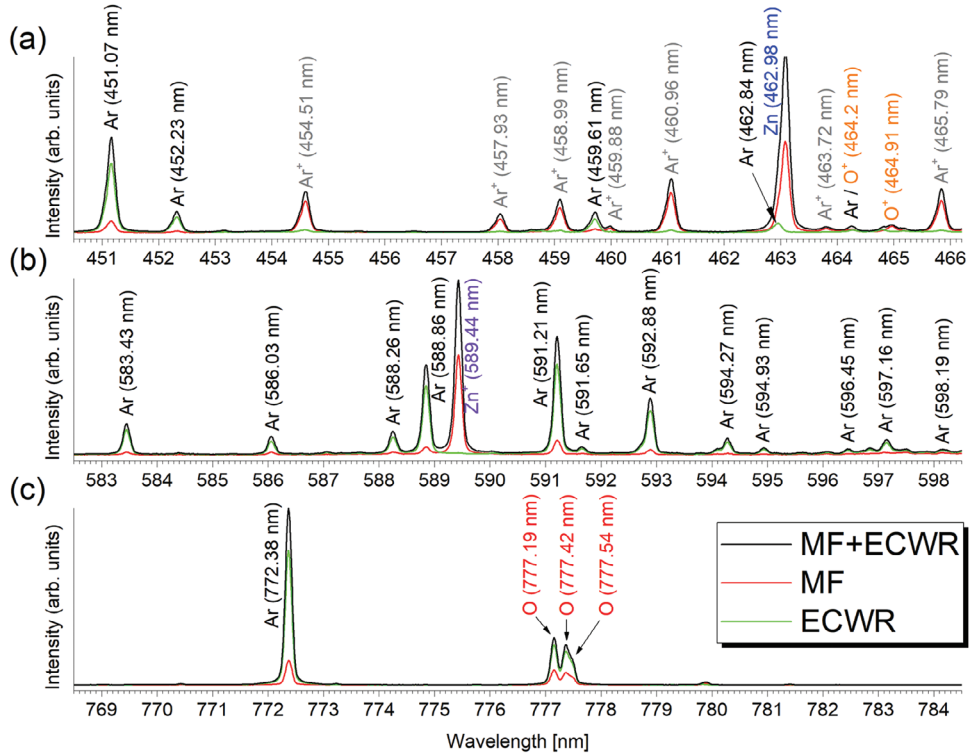

Figure 5. Optical emission spectra aids understanding of excellent properties of films. Optical emission spectra in the wavelength range of a) 450–466 nm, b) 582–598 nm, and c) 768–784 nm taken during the deposition of the ZnO films under MF (red line), ECWR (green line) and MF+ECWR (black line) conditions. These are selected wavelength intervals of the emission spectrum with clearly visible strong lines of individual particles: Ar, Ar^+, Zn, Zn^+, O and O^+. The intensities in all 3 spectra are normalized with respect to the intensity of the strongest line in the given interval.

are significantly more intense compared to the films deposited by MF. The more intense luminescence is attributed to collaborative contributions of better crystallinity, improved transparency, and lower self-absorption of the 382 nm luminescence emission for the MF+ECWR-deposited films compared to the MF-deposited films. On the other hand, the broad luminescence in the visible wavelength region, known to originate from defects (vacancies, interstitials, and their complexes) serving as luminescence centers, is more intense in the films deposited by MF. Raman spectroscopy confirmed that the MF-deposited films have a higher concentration of defects, compared to the MF+ECWR-deposited films. The time-resolved spectra of the UV luminescence obtained from streak camera images show luminescence profiles that feature ultrafast ps decay times, ranging from ≈27 ps for MF+ECWR-deposited films to as fast as 9 ps for MF-deposited films. Optical emission spectroscopy revealed that the high degree of dissociation of molecular oxygen together with an increased proportion of activated zinc particles contributes not only to a higher deposition rate of ZnO in the MF+ECWR magnetron, but especially to better crystallinity, fewer defects, and a lower proportion of oxygen vacancies, eventually leading to the superior UV luminescence of the MF+ECWR-deposited films. The intense UV luminescence together with the suppressed defect-related visible luminescence and ultrafast decay times paves the way for the progress in ultrafast timing for the development of time-of-flight detectors, high-resolution nuclear imaging cameras, and high-rate ultrafast timing devices.

4. Experimental Section

Deposition of ZnO Films by MF and MF+ECWR Magnetron: All deposition experiments were conducted in an ultra-high vacuum (UHV) stainless steel chamber with total volume of 30 dm^3 utilizing hybrid MF+ECWR deposition system (Figure 1a). Crystalline quartz (for transmittance and absorption characterization) and soda-lime glass (SLG) were used as substrates for the deposition of the ZnO films. The SLG substrates are microscope slides from Menzel-Gläser, Thermo Scientific, Braunschweig, Germany. The size of the SLG substrates is 20 mm x 20 mm with a thickness of 1 mm. The chamber was continuously pumped by a turbo-molecular pump with a nominal pumping speed of 300 l/s (Turbovac MAG W300) and a rotary vane pump with a pumping speed of 25 $m^3\ h^{-1}$. Before deposition, the chamber was pumped to a $p_b = 1 \times 10^{-4}$ Pa base pressure and during all deposition experiments, the chamber was kept at a constant 0.29 Pa pressure. Argon and oxygen gas flows were introduced into the chamber through the gas flow controllers. Their flow rates were held constant at $Q_{Ar} = 15$ sccm and $Q_{O2} = 10$ sccm for all the deposition conditions. The substrate was fixed on a rotating holder, rotating at a speed of 3 rpm, maintaining a distance of 10 cm between the target and the substrate. The substrates were heated to 300 °C during deposition and were left unannealed after deposition.

The deposition system is equipped with a 2-inch magnetron with circular planar cathodes having a 50-mm diameter. The target with a thickness of 3 mm was made of pure zinc with a purity of 99.9% (Plasmaterial). The magnetron was connected to a bipolar pulse power supply with a medium frequency of $f = 40$ kHz. The total absorbed MF power during all experiments was $P_{MF} = 300$ W. Placed between the magnetrons and the substrates is a water-cooled RF ICP coil with a 200-mm diameter. A PECWR power of 200 W was introduced to the ICP coil, and this power was maintained during the deposition process for the MF+ECWR films.

Table 1. Deposition conditions used for the preparation of selected ZnO samples: deposition time, working pressure, flow rates of working gases O_2 and Ar, MF power to the magnetron, power absorbed in the ECWR electrode, film thickness and corresponding deposition rate.

Sample name	Time (min)	P (Pa)	Q_{O2} (sccm)	Q_{Ar} (sccm)	P_{MF} (W)	P_{ECWR} (W)	Thickness (nm)	Dep. rate(nm/min)
MF (2.2 μm)	43	0.29	10	15	300	0	2200	51
MF (4.7 μm)	86	0.29	10	15	300	0	4700	55
MF+ECWR (3.0 μm)	22	0.29	10	15	300	200	3000	136
MF+ECWR (5.7 μm)	43	0.29	10	15	300	200	5700	133

A static homogeneous magnetic field with an induction of ≈1.7 mT was introduced into the ECWR electrode region using a Helmholtz coil in order to bring the system close to ECWR resonance. The current and voltage waveforms for both MF and MF+ECWR conditions are shown in Figure S7 (Supporting Information). The total deposition time was set between 22 to 86 min based on the deposition rate and the required thickness of the ZnO layer. A complete overview of the conditions used during deposition is summarized in **Table 1**. As other deposition experiments showed, the process window is relatively narrow, because a small deviation from the values in Table 1 (e.g., a change in the Ar/O_2 ratio from 10/15 to 15/15, or a change in PECWR by more than 30%) led to a radically lower intensity of UV luminescence.

Characterization of ZnO Films Deposited by MF and MF+ECWR Magnetron: The thickness of the ZnO films were measured using cross-sectional scanning electron microscopy (SEM) with an electron beam energy of 5 keV (Tescan FERA 3) and verified by a surface profilometer (Tencor, Alpha Step 500). The surface morphology of the films was evaluated using the same SEM with an operating voltage of 5.0 kV. Grazing incidence x-ray diffractometry (GIXRD) in reflection geometry with a grazing incidence angle of $\omega = 2.5°$ was used to determine the crystallinity of the films (Empyrean x-ray diffractometer). The diffractometer used a wavelength λ of 0.154 nm (Cu Kα radiation). The measurement was performed with a 2θ range from 10° to 90° with a 0.01° step size. A software package (PANanalytical HighScore Plus 4.0) was used for qualitative analysis of the diffraction patterns. A transmission electron microscope (TEM) was used to analyze the films' cross-sectional microstructure. For this purpose, the cross-section of the film was exposed using a focused ion beam (FIB) microscope (JEM-9320). The FIB microscope was operated using 30 kV Ga^+ ion beams after applying a 1 μm carbon coating on the film's surface. Microstructures of the films' cross-sections were observed using an atomic resolution analytical electron microscope (JEOL JEM-ARM200F ACCELARM) operated at 200 kV. Raman spectroscopy was performed in the back-scattering configuration using the polarized beam of an Ar ion laser operating at 514.5 nm wavelength (Renishaw Raman Microscope RM 1000). The total area illuminated by the laser beam was 4 μm^2.

The transmission spectra of the ZnO films were obtained using a UV–vis-NIR spectrophotometer (HITACHI U-4100). The PL emission spectra and decay time of the ZnO films were obtained by exciting the films with the 290-nm emission (third harmonic) of a mode-locked Ti:sapphire laser operating at the fundamental wavelength of 870 nm (Tsunami Oscillator and Spitfire Regenerative Amplifier, Spectra Physics). The laser pulses have a 100-fs pulse duration, 20-mJ pulse energy, and 1 kHz repetition rate. To measure the spectra and intensity of PL, the emission from the film was collected and focused onto a fiber spectrometer (StellarNet UV) with a 1200 g mm^{-1} grating efficiency from 200 to 600 nm. To measure the decay time of PL, the emission from the film was collected and focused using a quartz lens onto the entrance slit of a spectrograph. The spectrograph has a focal length of 25 cm and a groove density of 600 gr mm^{-1}. It was coupled to a streak camera unit (HAMAMATSU C1587) and a CCD camera. The absolute quantum yield of the UV PL was measured using a UV-NIR absolute PL quantum yield spectrometer (Quanturus-QY PlusC13534-11, Hamamatsu Photonics K.K) equipped with a 150-W xenon light source providing excitation in the 250 – 850 nm wavelength range and a BT-CCD linear image sensor with a measurement wavelength range from 200 to 950 nm. Cathodoluminescence (CL) spectra and SEM images of the CL cross-sections were measured using a JEOL JSM-7800F Schottky Field Emission Scanning Electron Microscope equipped with a CL detector (Gatan MonoCL4Elite). The accelerating voltage was 5 kV. For this purpose, the cross-sections were polished using a cross-section polisher (JEOL IB19520CCP). The cross-section polisher was operated using 8 keV Ar ion beams. All measurements were taken at room temperature.

Supporting Information

Supporting Information is available from the Wiley Online Library or from the author.

Acknowledgements

This work was supported by the Czech Academy of Sciences (MPP project no. JSPS-23-07), the JSPS KAKENHI Grant Number 21K18909, the JSPS Bilateral Program Grant Number JPJSBP120232502, the Amada Foundation (Grant No. AF-2022230-B3) and Hibi Science Foundation, the Catalyst: Seeding fund provided by the New Zealand Ministry of Business, Innovation, and Employment and administered by the Royal Society Te Apārangi (CSG-MAU2003), and the Osaka University Institute of Laser Engineering Collaborative Research Fund (2023B1-003). The authors would like to thank Takashi Matsubara from the Nagoya Institute of Technology for his help in FIB and Dr. Yoko Sakurai from the Nagoya Institute of Technology for her help in SEM and CL measurements.

Open access publishing facilitated by Fyzikalni ustav Akademie ved Ceske republiky, as part of the Wiley - CzechELib agreement.

Conflict of Interest

The authors declare no conflict of interest.

Author Contributions

M.C.-R. and J.O. performed conceptualization, methodology, investigation, formal analysis, discussion of results, wrote the original draft, visualization, project administration, funding acquisition. K.H., Y.M., and A.P. performed investigation, formal analysis, visualization. K.S., L.V., T.A., M.K., Y.A. performed investigation. Z.J. performed visualization. M.N., J.A.H., and N.S. provided resources, and supervised. R.H. performed investigation, formal analysis, discussion of results. S.O. performed conceptualization, investigation, discussion of results, resources, funding acquisition, wrote the original draft, and supervision. Z.H. performed conceptualization, methodology, investigation, discussion of results, resources, wrote, reviewed and edited, supervision. K.Y. performed investigation, discussion of results, resources, funding acquisition, project administration, wrote, reviewed and edited, supervision. All authors discussed and commented on the final manuscript.

Data Availability Statement

The data that support the findings of this study are available from the corresponding author upon reasonable request.

Keywords

electron cyclotron wave resonance, medium-frequency range magnetron sputtering, thin film, UV, zinc oxide

Received: March 8, 2024
Revised: April 25, 2024
Published online: May 10, 2024

[1] T. K. Lewellen, *Semin. Nucl. Med.* **1998**, *28*, 268.
[2] Y. Arikawa, T. Nagai, Y. Abe, S. Kojima, S. Sakata, H. Inoue, M. Utsugi, Y. Iwasa, T. Murata, N. Sarukura, M. Nakai, H. Shiraga, S. Fujioka, H. Azechi, *Rev. Sci. Instrum.* **2014**, *85*, 11E125.
[3] S. Kwon, R. Ota, E. Berg, F. Hashimoto, K. Nakajima, I. Ogawa, Y. Tamagawa, T. Omura, T. Hasegawa, S. R. Cherry, *Nat. Photon.* **2021**, *15*, 914.
[4] C. Dujardin, E. Auffray, E. Bourret-Courchesne, P. Dorenbos, P. Lecoq, M. Nikl, A. N. Vasil'ev, A. Yoshikawa, R.-Y. Zhu, *IEEE Trans. Nucl. Sci.* **2018**, *65*, 1977.
[5] M. Nikl, *Meas. Sci. Technol.* **2006**, *17*, R37.
[6] H. Chen, Z. Jiang, H. Hu, B. Kang, B. Zhang, X. Mi, L. Guo, C. Zhang, J. Li, J. Lu, L. Yan, Z. Fu, Z. Zhang, H. Zheng, H. Xu, *Nat. Photon.* **2022**, *16*, 651.
[7] M. J. F. Empizo, Y. Minami, K. Yamanoi, T. Shimizu, M. Yoshimura, N. Sarukura, T. Murata, A. Yamaji, A. Yoshikawa, M. Guzik, Y. Guyot, G. Boulon, M. Cadatal-Raduban, *J. Alloys Compd.* **2021**, *856*, 158096.
[8] Y. Minami, J. L. Gabayno, V. C. Agulto, Y. Lai, M. J. F. Empizo, T. Shimizu, K. Yamanoi, N. Sarukura, A. Yoshikawa, T. Murata, M. Guzik, Y. Guyot, G. Boulon, J. A. Harrison, *J. Non-Cryst. Solids* **2019**, *521*, 119495.
[9] L. Li, T. Li, Y. Hu, C. Cai, Y. Li, X. Zhang, B. Liang, Y. Yang, J. Qiu, *Light Sci. Appl.* **2022**, *11*, 51.
[10] M. Laval, M. Moszynski, R. Allemand, E. Cormoreche, P. Guinet, R. Odru, J. Vacher, *Nucl. Instrum. Methods Phys. Res.* **1983**, *206*, 169.
[11] R. H. Pots, E. Auffray, S. Gundacker, *Front. Phys.* **2020**, *8*, 592875.
[12] S. Gundacker, R. H. Pots, A. Nepomnyashchikh, E. Radzhabov, R. Shendrik, S. Omelkov, M. Kirm, F. Acerbi, M. Capasso, G. Paternoster, A. Mazzi, A. Gola, J. Chen, E. Auffray, *Phys. Med. Biol.* **2021**, *66*, 114002.
[13] J.-C. Deinert, D. Wegkamp, M. Meyer, C. Richter, M. Wolf, J. Stähler, *Phys. Rev. Lett.* **2014**, *113*, 057602.
[14] C. Bauer, G. Boschloo, E. Mukhtar, A. Hagfeldt, *Chem. Phys. Lett.* **2004**, *387*, 176.
[15] J. Wilkinson, K. B. Ucer, R. T. Williams, *Nucl. Instrum. Methods. Phys. Res. B* **2005**, *537*, 66.
[16] M. Tanaka, M. Nishikino, H. Yamatani, K. Nagashima, T. Kimura, Y. Furukawa, H. Murakami, S. Saito, N. Sarukura, H. Nishimura, K. Mima, Y. Kagamitani, D. Ehrentraut, T. Fukuda, *Appl. Phys. Lett.* **2007**, *91*, 231117.
[17] Y. Furukawa, M. Tanaka, T. Nakazato, T. Tatsumi, M. Nishikino, H. Yamatani, K. Nagashima, T. Kimura, H. Murakami, S. Saito, N. Sarukura, H. Nishimura, K. Mima, Y. Kagamitani, D. Ehrentraut, T. Fukuda, *J. Opt. Soc. Am. B* **2008**, *25*, B118.
[18] M. Kano, A. Wakamiya, K. Sakai, K. Yamanoi, M. Cadatal-Raduban, T. Nakazato, T. Shimizu, N. Sarukura, D. Ehrentraut, T. Fukuda, *J. Cryst. Growth* **2011**, *318*, 788.
[19] Z. Lin, S. Lv, Z. Yang, J. Qiu, S. Zhou, *Adv. Sci.* **2022**, *9*, 2102439 .
[20] H. Wu, Q. Wang, Ao Zhang, G. Niu, M. Nikl, C. Ming, J. Zhu, Z. Zhou, Yi-Y Sun, G. Nan, G. Ren, Y. Wu, J. Tang, *Sci. Adv.* **2023**, *9*, eadh1789.
[21] A. Yamamoto, T. Kido, T. Goto, Y. Chen, T. Yao, A. Kasuya, *J. Cryst. Growth* **2000**, *214*, 308.
[22] M. Lorenz, R. Johne, T. Nobis, H. Hochmuth, J. Lenzner, M. Grundmann, H. P. D. Schenk, S. I. Borenstain, A. Schön, C. Bekeny, T. Voss, J. Gutowski, *Appl. Phys. Lett.* **2006**, *89*, 243510.
[23] Ü. Özgür, A. Teke, C. Liu, S.-J. Cho, H. Morkoç, *Appl. Phys. Lett.* **2004**, *84*, 3223.
[24] T. Koyama, S. F. Chichibu, *J. Appl. Phys.* **2004**, *95*, 7856.
[25] *Physical Measurement Laboratory*, National Institute of Standards and Technology, Gaithersburg, Maryland 20899, USA https://physics.nist.gov/cgi-bin/ffast/ffast.pl?Z=64&Formula=ZnO&gtype=5&&=U&lower=&upper=&density=5.61.
[26] X. Zhao, D. Huang, G. Li, Y. He, W. Peng, G. Li, *Sens. Actuators, A* **2022**, *334*, 113310.
[27] K. Kodama, T. Uchino, *J. Phys. Chem. C* **2014**, *118*, 23977.
[28] M. R. Wagner, G. Callsen, J. S. Reparaz, J.-H. Schulze, R. Kirste, M. Cobet, I. A. Ostapenko, S. Rodt, C. Nenstiel, M. Kaiser, A. Hoffmann, A. V. Rodina, M. R. Phillips, S. Lautenschläger, S. Eisermann, B. K. Meyer, *Phys. Rev. B* **2011**, *84*, 035313.
[29] D. P. Norton, Y. W. Heo, M. P. Ivill, K. Pearton, M. F. Chisholm, *Mater. Today* **2004**, *7*, 34.
[30] H. Oechsner, M. Scheib, H. Goebel, *Thin Solid Films* **1999**, *341*, 101.
[31] V. Stranak, A.-P. Herrendorf, S. Drache, M. Cada, Z. Hubicka, M. Tichy, R. Hippler, *Appl. Phys. Lett.* **2012**, *100*, 141604.
[32] Z. Hubička, M. Zlámal, J. Olejníček, D. Tvarog, M. Čada, J. Krysa, *Coatings* **2020**, *10*, 232.
[33] V. Stranak, A-P. Herrendorf, H. Wulff, S. Drache, M. Cada, Z. Hubicka, M. Tichy, R. Hippler, *Surf. Coat. Technol.* **2013**, *222*, 112.
[34] H. P. Klug, L. E Alexander. *X-ray Diffraction Procedures for Polycrystalline and Amorphous Materials*, Wiley Interscience, London, **1974**, 656.
[35] J. Reyes-Gasga, E. L. Martinez-Pineiro, G. Rodrigues-Alvares, G. E. Tiznado-Orozco, R. Garcia-Garcia, E. F. Bres, *Mater. Sci. Eng. C.* **2013**, *33*, 4568.
[36] D. N. Montenegro, V. Hortelano, O. Martínez, M. C. Martínez-Tomas, V. Sallet, V. Muñoz-Sanjosé, J. Jiménez, *J. Phys. D: Appl. Phys.* **2013**, *46*, 235302.
[37] Y. Song, S. Zhang, C. Zhang, Y. Yang, K. Lv, *Crystals* **2019**, *9*, 395.
[38] J. Sann, J. Stehr, A. Hofstaetter, D. M. Hoffmann, A. Neumann, M. Lerch, U. Haboek, A. Hoffmann, C. Thomsen, *Phys. Rev. B* **2007**, *76*, 195203.
[39] The International Centre for Diffraction Data – ICDD, https://www.icdd.com/.
[40] Y. F. Chen, D. M. Bagnall, H. Koh, K. Park, K. Hiraga, Z. Zhu, T. Yao, *J. Appl. Phys.* **1998**, *84*, 3912.
[41] W. Shan, W. Walukiewicz, J. J Song, *Appl. Phys. Lett.* **2005**, *86*, 191911.
[42] Y. G. Wang, S. P. Lau, H. W. Lee, S. F. Yu, B. K. Tay, X. H. Zhang, H. H. Hng, *J. Appl. Phys.* **2003**, *94*, 354.
[43] R. Khokhra, B. Bharti, H-No Lee, R. Kumar, *Sci. Rep.* **2017**, *7*, 15032.
[44] H. S. Kang, J. S. Kang, J. W. Kim, S. Y. Lee, *J. Appl. Phys.* **2004**, *95*, 1246.
[45] M. Berseth, B. G. Svenson, A. Yu. Kuznetsov, P. Klason, Q. X. Zhao, M. Willander, *Appl. Phys. Lett.* **2006**, *89*, 262112.
[46] X. L Wu, G. G. Siu, C. L. Fu, *Appl. Phys. Lett.* **2001**, *78*, 2285.
[47] A. B. Djurisic, Y. H. Leung, K. H. Tam, Y. F. Hsu, L. Ding, W. K. Ge, Y. C. Zhong, K. S. Wong, W. K. Chan, H. L. Tam, K. W. Cheah, W. M. Kwok, D. L. Phillips, *Nanotechnology* **2007**, *18*, 095702.
[48] R. Yukawa, S. Yamamoto, R. Arita, Y. Minami, K. Yamanoi, K. Ozawa, K. Sakamoto, T. Shimizu, N. Sarukura, I. Matsuda, *Phys. Rev. Mater.* **2022**, *6*, 104607.
[49] P. Sezemský, V. Straňák, J. Kratochvíl, M. Čada, R. Hippler, M. Hrabovský, Z. Hubička, *Plasma Sources Sci. Technol.* **2019**, *28*, 115009.
[50] V. Stranak, J. Kratochvil, J. Olejnicek, P. Ksirova, P. Sezemsky, M. Cada, Z. Hubicka, *J. Appl. Phys.* **2017**, *121*, 171914.